Freezing of dilute aqueous-alcohol nanodroplets: the effect of molecular structure

Tong Sun[a] and Barbara E. Wyslouzil*[ab]

[a] William G. Lowrie Department of Chemical and Biomolecular Engineering, The Ohio State University, Columbus, Ohio 43210, USA.

[b] Department of Chemistry, The Ohio State University, Columbus, Ohio 43210, USA.

Abstract:

We investigate vapor-liquid nucleation and subsequent freezing of aqueous-alcohol nanodroplets containing 1-pentanol, 1-hexanol and their 3- isomers. The aerosols are produced in a supersonic nozzle, where condensation and freezing are characterized by static pressure and Fourier Transform Infrared spectroscopy measurements. At fixed water concentrations, the presence of alcohol enables particle formation at higher temperatures since both the equilibrium vapor pressure above the critical clusters and the cluster interfacial free energy are decreased relative to the pure water case. The disappearance of a small free OH peak, observed for pure water droplets, when alcohols are added and shifts in the CH peaks as a function of alcohol chain length reveal varying surface partitioning preferences of the alcohols. Changes in the FTIR spectra during freezing, as well as changes in the ice component derived from self modelling curve resolution analysis, show that 1-hexanol and 1-pentanol perturb freezing less than their branched isomers. This behavior may reflect the molecular footprints of the alcohols, the available surface area of the droplets, and not only alcohol solubility. The presence of alcohols also lowers the freezing temperature relative to that of pure water, but when there is clear evidence for the formation of ice, the ice nucleation rates change by less than a factor of ~2-3 for all cases studied.

I. Introduction

Organic matter comprises 20-90% of the fine aerosol mass depending on the global location,[1,2] and understanding the role of organic compounds in these particles is important to predicting cloud formation and radiative climate forcing.[3–7] Amphiphilic molecules, with their hydrophilic and hydrophobic regions, can alter the interfacial properties of the aerosol particles by segregating to the surface. For aqueous-organic aerosol particles in the nanometer size regime, this can result in very different chemical compositions in the bulk and surface regions.[8–12] Significant research effort has been directed toward understanding this partitioning and role it plays in atmospheric processes,[13,14] including the activation of cloud condensation nuclei,[15–17] but less effort has been directed toward understanding how such partitioning may affect freezing.[18] The *n*-alcohols are among the simplest amphiphilic molecules present in the atmosphere and their properties are easily tuned by increasing the length of the hydrophobic tail or by changing the location of the hydrophilic –OH group. Thus, understanding how these changes affect ice formation is a first step to understanding the role more complex amphiphiles in the environment may have on this process.

Experiments have studied the bonding and ordering of alcohols at the vapor/liquid interface of

aqueous solutions,[9,19–26] and probed how the H-bonding network in aqueous solutions is perturbed by the presence of short-chain alcohols,[27–31] although the water structure around alcohols remains debated. Surface tension measurements show a more rapid decrease in the surface tension with molar concentration as the alcohol chain length increases, indicating that the alcohols with longer alkyl tail are more surface-active.[32,33] X-ray photoelectron spectroscopy (XPS) measurements of the C2 to C4 alcohols find lower attenuation of the C 1s signal of the aliphatic carbon relative to the carbon in the hydroxyl group, consistent with these molecules orienting so that the hydrophilic functional group points toward the surface.[26] At higher surface coverage, Van der Waal's interactions between the alkyl tails of linear alcohols favor the dehydration of the alcohol molecules on the surface,[34] and stronger interactions lead to an increasing surface propensity as the chain length increases.[25,26] Vibrational sum frequency (VSF) measurements show that the size of the hydrophobic region of the linear alcohols enhances the H-bonding and alters net H orientation of water at the interface from down to up upon changing the alcohols from shorter than propanol to longer than pentanol.[35] The crossover effect is attributed to the negatively-charged electric field induced by the adsorption of OH^- at the interface. Molecular structure also affects surface partitioning with linear alcohols (C4-C6) having higher surface concentration than their branched isomers.[36] VSF measurements of linear alcohols ($C \geq 8$) show almost no conformational disorders at the water/air interface whereas the 2 or 3-position isomers pack less efficiently and appear to have gauche defects.[37] With two alkyl segments pointing outward from the bulk aqueous phase, the branched alcohols necessarily have a larger molecular footprint than the 1-alcohols. For the C4 to C6 alcohols, fits of XPS data to a Langmuir isotherm found that at monolayer coverage, the packing of linear alcohols is about 50% higher than their branched counterparts.[25]

In our recent work,[18] we investigated the freezing of dilute aqueous-alcohol nanodroplets containing 1 to 6 mol% 1-propanol or 1-pentanol. Although the overall concentration of these droplets is significant – for 1-pentanol nanodroplets the overall concentration was well beyond the bulk solubility limit at room temperature (Table 1) – partitioning calculations suggest that most of the alcohol resides on the surface.[18] Thus, the large surface to volume ratio of the nanodroplets ensures that the concentration of the water-rich interior is both dilute (<~0.021 mole fraction for 1-propanol; < ~0.003 mole fraction for 1-pentanol) and well below the room temperature solubility limit for 1-pentanol.

In our earlier paper, we quantitatively analyzed the temperature dependent FTIR spectra using self modelling curve resolution (SMCR).[18] We observed that below a critical alcohol concentration – ~4 mol% for the fully miscible 1-propanol and ~5 mol % for the partially miscible 1-pentanol – ice nucleation kinetics were only slightly perturbed from those of pure water. Furthermore, the solute-correlated ice component (IC) spectrum, derived from two rounds of SMCR analysis, was identical to that of pure water suggesting that the ice formed in the mixed droplets was identical to that formed in pure water droplets. Above this critical alcohol concentration, the IC was broader and peaked at a higher wavenumber suggesting a less ordered structure than pure ice, perhaps a glassy state, had formed. These observations, together with predictions of a simple partitioning model, suggest that at the lowest alcohol concentrations most of the alcohol resides on the surface where it neither enhances nor impedes

ice nucleation. For 1-pentanol, the transition from an IC essentially identical to that of pure water to one that is clearly not, corresponds to an alcohol mole fraction where simple geometric arguments suggest the surface has become saturated with alcohol. Thus, at higher mole fractions alcohol molecules are forced into the droplet interior where they can interfere with the formation of ice. Finally, based on the partitioning model and the experimental results, when the estimated mole fractions of alcohol in the droplet interior (the bulk mole fractions rather than the overall mole fractions) are equal, 1-pentanol perturbs ice nucleation more than 1-propanol consistent with 1-pentanol's larger molecular volume.

In the current paper, we extend our work to focus on the effect of molecular structure. For the 1– and 3– isomers of pentanol and hexanol we investigate how changing the location of the -OH group influences aerosol freezing. As detailed in Table 1, these isomers differ in their water solubility (see also Figure S1), surface activity, and molecular footprint at the liquid-vapor interface. If, as suggested by our earlier work,[18] freezing is only perturbed once the overall alcohol concentration in a nanodroplet droplet is higher than that required to form a monolayer on the surface, we would expect molecular footprint to be an important factor in addition to solubility in determining the concentration at which ice formation is affected. For the C5/C6 alcohols investigated here, the 3-isomers should perturb freezing at lower overall mole fractions than the corresponding 1-isomers both because they are more soluble and because their molecular footprint is larger. Of particular interest is whether 3-hexanol perturbs freezing more readily than the more soluble 1-pentanol.

Table 1: Key properties of the alcohols.

Alcohol	Solubility at 283 K (mole fraction)[38]	Surface tension at 283 K (mN/m)[39]	Molecular area at monolayer coverage at 283 K (nm^2)[25]
1-propanol	Fully soluble	24.5	--
1-pentanol	0.0054	26.2	0.41
3-pentanol	0.0151	26.0	0.63
1-hexanol	0.0013	27.0	0.44
3-hexanol	0.0035	25.4	0.60

The paper is organized as follows. In Section II, we describe the experiments and data analysis methods. Section III presents and discusses the results, leading to the summary and conclusions in Section IV.

II. Experimental

Aqueous-alcohol nanodroplets are generated by vapor-liquid nucleation and condensation as a dilute vapor-carrier gas mixture flows through a supersonic nozzle. The apparatus and nozzle

used here (Figure S2) are the same as in our earlier work. To summarize, nitrogen carrier gas is drawn from the gas side of three high pressure liquid nitrogen Dewars, warmed to room temperature, and each flow is controlled by a mass flow controller. The total N_2 flow through the system is ~ 525 g/min. Liquid water and alcohol are independently pumped into the system using peristaltic pumps, the liquids are vaporized by spraying them into hot carrier gas, and the flow rates are monitored using balances. For all of the experiments (including those in Ref. 18) the water flow rate was maintained close to 5.5 g/min to yield initial mole fractions $y_{0,\mathrm{H_2O}}$ ranging from 0.0159 to 0.0169 with respect to all the entering materials, or equivalently initial water partial pressures $p_{0,\mathrm{H2O}}$ ranging from 0.95 to 1.01 kPa. Variability in these parameters for a particular experiment is ~ 2%. The alcohol mole fraction, relative to the total amount of condensable material, $x_2 = \frac{y_{0,\mathrm{alcohol}}}{y_{0,\mathrm{alcohol}}+y_{0,\mathrm{H_2O}}}$ is varied from ~0.01 to ~0.06. The use of excess carrier gas ensures the fluid dynamics are described accurately by the equations describing supersonic flow in the presence of heat addition. Since the partial pressure of N_2 is always well below its equilibrium vapor pressure, it does not condense or otherwise interfere with the phase transitions of the condensable materials.[40] The stagnation pressure p_0, maintained at 60.0±0.2 kPa, is measured at the entrance of the nozzle via a pressure tap and corrected for the kinetic energy of the flow. The stagnation temperature T_0, set to 35.0±0.2 °C, is controlled by a water bath and monitored by a platinum resistance temperature detector near the nozzle entrance.

The nozzle (Figure S2) is a sandwich design with flat side walls and contoured top and bottom blocks that create the converging (subsonic) and diverging (supersonic) regions of the nozzle. The area of the nozzle throat A^* is 0.635 cm^2 and the effective expansion rate $d(A(z)/A^*)/dz$ is ~0.086 cm^{-1}, where $A(z)$ is the cross-sectional area z cm downstream of the effective throat (z = 0). This expansion rate generates cooling rates on the order of 5×10^5 K/s. The parallel sidewalls are 1.27 cm apart and each contains a 14.5 cm long × 1.2 cm high × 0.3 cm thick CaF_2 window for optical access.

In the absence of condensation, the pressure and temperature of the expanding gas decrease monotonically from the entrance to the exit of the nozzle. When enough condensable material is present, droplets form via homogeneous nucleation in the supersonic region of the nozzle. The heat released to the flow by droplet growth increases the temperature of the flow and quenches particle formation in ~ 10 μs. Once droplet growth is complete, the temperature decreases again and once the temperature is low enough, droplets can freeze. At the nozzle exit the gas mixture is exhausted to atmosphere by two rotary vane vacuum pumps.

For the low alcohol concentrations used in the current experiments, small angle X-ray scattering (SAXS) measurements[41] found that the average particle size $\langle r \rangle$ of water–n-pentanol droplets was 6.0 ± 0.5 nm and essentially independent of the pentanol concentration (see also Figure S15 of ref. 18). This is because the size of the particles is largely controlled by the water partial pressure, a value that is constant in the experiments. Thus, we assume the characteristic size for the particles in all the experiments is $\langle r \rangle = 6$ nm.

A. Pressure trace measurements

In a pressure trace measurement, the static pressure is recorded using a probe that moves along the axis centerline from a point upstream of the throat to near the nozzle exit. Pressure measurements are taken every 0.1 cm in the subsonic region (-1.0 cm < z < -0.2 cm), every 0.04 cm near the throat (-0.2 cm < z < 0.2 cm), every 0.1 cm up to z = 2.6 cm, and then every 0.2 cm to the end of the nozzle (z~10.3 cm). Since the energy released by a phase transition raises both the temperature and static pressure of the flow, the presence of condensation can be detected by comparing the pressure trace measured for the carrier gas-condensable mixture (wet trace) with that measured for pure nitrogen after correcting for the differences in mixture heat capacity (isentrope). The measured pressures are interpolated to generate data points every 0.01 cm. Assuming that the area ratio $A(z)/A^*$ is not affected by the condensation process, the remaining parameters of the flow, *i.e.* temperature, velocity, density and mass fraction of the condensate can be determined by integrating the supersonic flow equations with heat addition.[42] Under our operating conditions, however, condensation can compress the boundary layers that develop along the nozzle walls relative to those that develop under the isentropic flow conditions.[43] To improve the estimates of the flow parameters we therefore integrate the flow equations using pressure p and mass fraction of condensate g as input where the latter are derived from an integrated analysis of small angle X-ray scattering measurements and pressure trace measurements in the same nozzle under similar operating conditions and water partial pressures ($p_{0,H2O}$ = 1.05 kPa).[41,44]

B. FTIR

The liquid to solid phase transition is detected by position-resolved FTIR measurements that monitor the OH stretch band of hydrogen bonded H_2O in the wavenumber range of 3000-3600 cm^{-1}. The presence of the alcohols is detected by monitoring the CH stretch band in the wavenumber range of 2800-3000 cm^{-1}.

The IR beam is guided through the nozzle by two focusing mirrors and one plane mirror and is detected by a liquid nitrogen cooled MCT detector (Figure S2). At each position, 32 spectra are measured with no apodization and a resolution of 1 cm^{-1}. The water/CO_2 suppression function is turned on to minimize the influence of room air on the spectra. The background spectrum corresponds to a pure nitrogen flow is measured immediately prior to measuring the sample spectrum. Since the flow expands and the mass fraction of condensate can change as a function of position, the spectra are normalized using the following equation

$$\varepsilon_a(\nu) = -\log\left(\frac{I_s(\nu)}{I_e(\nu)}\right) * \frac{\bar{m}}{l\rho g} \qquad (1)$$

where $I_s(\nu)$ denotes the measured intensity of light passing through the mixture (the sample), $I_e(\nu)$ is the measured intensity of light passing through the carrier gas only (the background), $\bar{m}$ denotes the molecular weight of the condensate, l is the beam path length, i.e. the nozzle block width, ρ is the flow density calculated from the PTM, and g is the mass fraction of condensate. The units of $\varepsilon_a(\nu)$ are $\frac{\mathrm{m}^2}{\mathrm{mol}}$.

C. SMCR analysis and freezing kinetics

To further quantify the effect of alcohols on aerosol freezing, we performed two rounds of self modelling curve resolution (SMCR) analysis on each set of temperature dependent FTIR spectra corresponding to a fixed value of x_2. Each round of SMCR decomposes a set of spectra into linear combinations of two non-negative, linearly independent underlying component spectra without placing constraints on the corresponding spectral shapes.

In the first round of SMCR, we take the spectrum measured at ~231 K as one of the first-round component spectra and call this the "high temperature liquid" reference component spectrum (HTL). A pairwise analysis decomposes the remaining spectra into linear combinations of the HTL and the corresponding SMCR low temperature component spectrum. This is the same approach taken to treat temperature dependent Raman spectra of water as mixtures of high and low temperature spectral components.[45–47] In our case prior to the initiation of freezing, the SMCR low temperature component spectra are all very similar, i.e. the shape is essentially independent of temperature. We refer to this spectrum as the "low temperature liquid" component (LTL). As the nanodroplets start to freeze, the shape of the SMCR low temperature component spectrum deviates from that of the LTL due to contributions from the emerging solid phase. After completing the first round of pairwise SMCR analysis, a joint analysis of all the "liquid-like" spectra yields a global estimate of the LTL.

In the second round of SMCR, we use the global LTL spectrum as one reference spectrum and decompose the low temperature SMCR spectra from the first round into linear combinations of the LTL and a second component spectrum that is assigned to the emerging frozen species. This new component is referred to as the "ice component" (IC). As demonstrated in Figure S8 of Ref. 18, the extracted ICs are robust to reasonable changes in the choice of the HTL and the temperature range used to determine the LTL. When the IC for the aqueous alcohol droplets is essentially the same as that of pure water (except in the CH stretch region) we assume that the droplets freeze to form pure water ice. SMCR analysis also yields the apparent ice fraction of each low temperature spectrum F'_{IC}. The fraction of the IC spectrum in the full spectrum, F_{IC}, is then found by multiplying F'_{IC} by the fraction of the LTL spectrum determined in the first-round analysis. If we assume that the IR cross section of the supercooled water and ice are the same, then F_{IC} also equals the mole fraction of ice in the aerosol. We expect, however, that F_{IC} is an upper bound on the true mole fraction of ice because the IR cross section of water decreases with decreasing hydrogen bond strength.

Finally, to quantify the freezing kinetics we assume that the aerosol is fully frozen at the lowest temperature achievable in the nozzle if F_{IC} approaches a constant value near the nozzle exit and the IC is close to that of pure water. For those cases we normalize F_{IC} to 1 to determine the fraction of fully frozen droplets F_F in the aerosol. The ice nucleation rate J_{ice} is related to the fraction of frozen droplets by

$$J_{\mathrm{ice}}\langle V\rangle = \frac{1}{t_2 - t_1} \ln\left(\frac{1-F_F(t_1)}{1-F_F(t_2)}\right), \qquad (2)$$

where $\langle V \rangle$ denotes the average droplet volume and *t* is the travel time of the aerosol relative to the effective throat. This analysis assumes that there is only one nucleation event within each droplet, nucleation occurs randomly within the volume of the droplet, and the time for one droplet to freeze is much less than that required for the whole aerosol to freeze.[48,49] Time *t* is related to position *z* by integrating $dt = dz/u(z)$, where $u(z)$ is the flow velocity.

D. Materials

The carrier gas nitrogen was boiled off from liquid nitrogen (purity of 99.998%) purchased from Praxair. The deionized water had a resistivity of ~18 megohm. The 3-pentanol (98%), 1-hexanol (>97%) and 3-hexanol (≥99%) were purchased from Sigma-Aldrich Corporation and used without further purification. The relevant physical properties are summarized in Table S1 of the Supplemental Information.

III. Results and Discussion

A. Pressure trace measurements

Pressure trace measurements for water condensing in the presence of 3-pentanol, 1-hexanol, and 3-hexanol were conducted as part of the current work. The experimental results for pure water, and water condensing in the presence of 1-propanol and 1-pentanol are available in Ref 18. These measurements provide the estimates for the position resolved temperature, velocity, and density of the flow that are used to characterize the onset of condensation, determine when condensation is essentially complete, translate between position and time, and normalize the IR spectra. As discussed in our earlier work,[43] the temperature accuracy of this approach is estimated to be ±2 K. The PTM analysis also assumes that the overall composition of the condensate matches that of the incoming vapor. This may not be strictly true for the rapidly growing aerosol, but once T = 220 K the vapor pressures of water and these alcohols above $\langle r \rangle \sim$ 6 nm droplets is consistent with over 97% of each species having condensed (Section SIII.B of Ref 18). Thus, at the low temperatures associated with freezing, the assumption is reasonable.

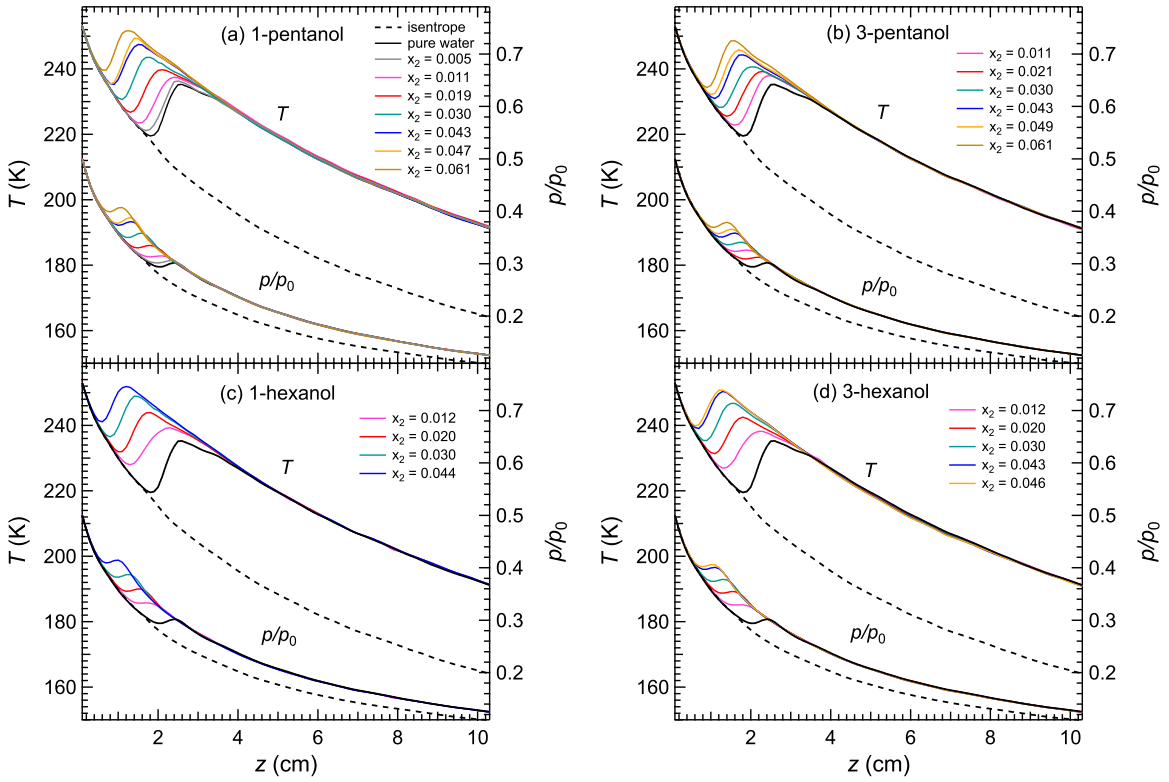

Figure 1 PTM results for water with (a) 1- pentanol [Reproduced from Ref. 18 with permission from the PCCP Owner Societies] (b) 3-pentanol, (c) 1-hexanol (d) 3-hexanol. The flowrate of water is fixed so that the partial pressure of water at the nozzle entrance $p_{v0,1}$= 0.98±0.03 kPa (averaged over all experiments). The flow rate of alcohol is then increased to achieve the noted mole fractions of condensable, x_2. As x_2 increases, condensation occurs at higher temperatures further upstream in the nozzle. The upper limit on x_2 is set by the need to maintain onset downstream of the throat (z=0).

Figure 1 illustrates the measured pressure and derived temperature profiles for the pure water and the C5 and C6 water-alcohol experiments and the results are summarized in Table 2. As the gas mixture expands across the nozzle, the temperature and pressure of the condensable flow initially match those of the expected isentropic expansion. Once the vapor-liquid nucleation rate is high enough, both variables deviate quickly from their respective isentropic values as heat is released to the flow by the rapidly growing droplets. Droplet formation is restricted to the region near the first local temperature minimum T_{min} (0.5 cm < z < 2 cm), and almost all the subsequent heat release is due to droplet growth. After rapid droplet growth ends, the temperature and pressure decrease again due to continued expansion of the flow and the droplet temperature rapidly equilibrates with that of the flow.[50,51] When the temperature is low enough, ice can nucleate and grow within the droplets.

Typically, water starts to freeze ~4 to 5 cm downstream of the throat. For this phase transition, however, heat release is not easily observed because (1) the heat of fusion is only about 10%

of the heat of vaporization and (2) the time scale over which ice nucleation occurs is nearly twice as long as the time scale associated with condensation.[18] Prior to freezing, the droplet temperature is essentially the same as that of the flow.[50,51] Once freezing starts, the stochastic nature of the process ensures only about 0.5% of the droplets are heated to temperatures higher than the flow at any given time. Thus, the average droplet temperature is perturbed by less than ~0.5 K (Section SIII.D of Ref. 18) and it is reasonable to assume that the aerosol temperature matches the flow temperature even during the liquid-to-solid phase transition.

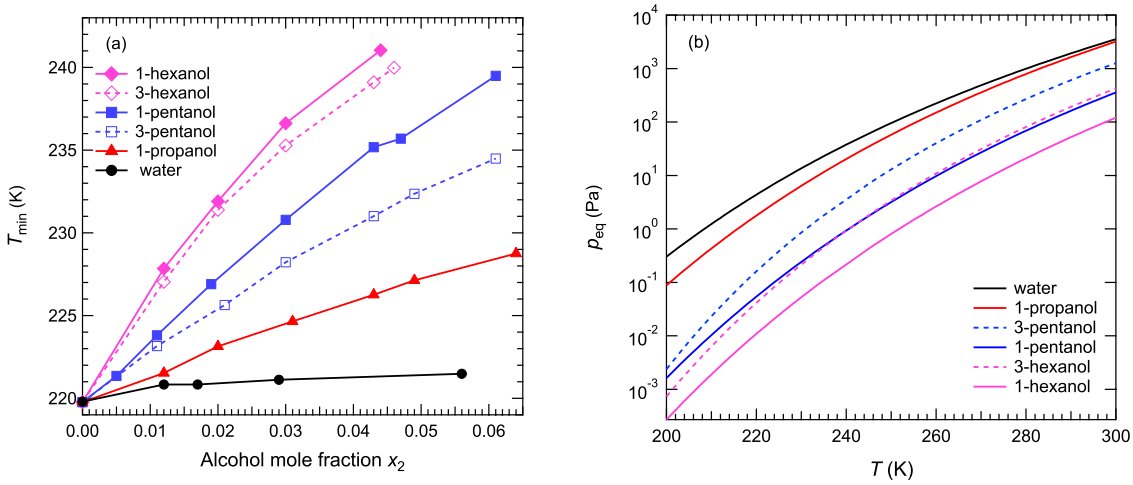

Figure 2 (a) $T_{\min,}$, the temperature that characterizes particle formation, is a strong function of the amount and type of alcohol added to the flow. The addition of comparable amounts of water has little effect on $T_{\min}$. **(b)** The equilibrium vapor pressures of water and the alcohols of interest roughly mirror the condensation behavior with higher values of $T_{\min}$ possible as the vapor pressure decreases. Data sources are documented in Table S1.

Changes in the onset of particle formation from the vapor phase observed in Figure 1 and Figure 2(a) can be understood within the framework of classical binary nucleation theory (CNT) as follows. The binary nucleation rate, J_{bin} can be written as

$$J_{\text{bin}} = K_{\text{bin}} \exp\left(-\frac{\Delta G^*_{\text{bin}}}{kT}\right), \qquad (3)$$

where K_{bin} is the kinetic prefactor, ΔG^*_{bin} is the change in the Gibbs free energy required to form a critical cluster (denoted by *) of the new condensed phase from the supersaturated vapor phase, k is the Boltzmann constant, and T is the temperature. In general, K_{bin} will not change much when a small amount of a second component is added, rather changes in rate are much more sensitive to changes in ΔG^*_{bin}. The change in the Gibbs free energy to form an arbitrary cluster of the new liquid phase from the supersaturated vapor is given by

$$\Delta G_{\text{bin}} = n_1 \Delta\mu_1 + n_2 \Delta\mu_2 + \sigma A, \qquad (4)$$

where n_i is the number of molecules of component i in the cluster, $\Delta\mu_i = \mu_{i,l} - \mu_{i,v}$ is the change in the chemical potential associated with the phase transition from the vapor to the liquid state, σ is the surface tension of the cluster, and A is its surface area. For the critical

cluster, i.e. that cluster in unstable equilibrium with the supersaturated vapor phase, $\Delta G^*_{\mathrm{bin}}$ can be written as

$$\Delta G^*_{\mathrm{bin}} = \frac{16\pi\sigma^{*3}v_m^{*2}}{(x_1^*\Delta\mu_1+(1-x_1^*)\Delta\mu_2)}, \qquad (5)$$

where v_m^* denotes the average molecular volume of the species comprising the critical cluster, and x_i^* is the bulk mole fraction of component i. Finally, the change in chemical potential can be written as

$$\Delta\mu_i = -kT\ln\frac{p_{v,i}}{p_{ve,i}(x_i)}, \qquad (6)$$

where $p_{v,i}$ is the partial pressure of component i in the gas phase and $p_{ve,i}(x_i)$ is the partial pressure of that species above a liquid phase with bulk composition x_i. Note that the thermodynamically consistent version of CNT accounts for differences in composition between the cluster surface and bulk.[52]

In supersonic nozzle experiments, $\Delta G^*_{\mathrm{bin}}$ is minimized very close to T_{min}. Thus, an easy way to compare the effect of different alcohols have on particle formation is to plot T_{min} as a function of the alcohol mole fraction x_2 as is done in Figure 2 (a). Clearly, T_{min} hardly changes on the addition of extra water, increases rapidly as the carbon chain length of the alcohol increases, and for a given chain length the 1-alcohols have a stronger effect on vapor phase nucleation than the 3-alcohols.

In the simplest case – the addition of a small amount of extra water – the change in chemical potential decreases slightly (becomes more negative) with the increase in water partial pressure whereas any changes in the surface tension and molecular volume, due to the small increase in temperature, are negligible. Thus, new particles can form at slightly higher temperatures leading to a small increase in T_{min}. This situation is similar to that observed for vapor phase nucleation from the highly ideal H_2O/D_2O systems.[53] In aqueous-alcohol systems, the trend of T_{min} reflects (1) the decrease in the vapor pressures of the alcohols with chain length and molecule structure (Figure 2 (b)), that lead to increases in the magnitude of $\Delta\mu_i$, and (2) the decrease in surface tension of the critical clusters due to the presence of the surface-active alcohol molecules. Furthermore, measurements and theory both find that at low alcohol concentrations critical clusters are enriched in alcohol relative to an ideal mixture at the same composition as the gas phase.[54,55] Since the critical clusters formed by vapor phase nucleation in supersonic nozzles typically contain fewer than ~10 molecules,[56] the addition of one or more alcohol molecules can have a significant effect on particle formation. In our experiments, where the water partial pressure is held constant, the addition of small amounts of alcohol therefore enables nucleation to occur at higher temperatures. The fact that 3-hexanol initiates nucleation more readily than 1-pentanol, even though the vapor pressures of these two molecules are rather similar, reflects the fact that in the temperature range of interest, 220-240 K, the surface tension of 3-hexanol is lower than that of 1-pentanol.[39]

B. FTIR: Trends and basic interpretation

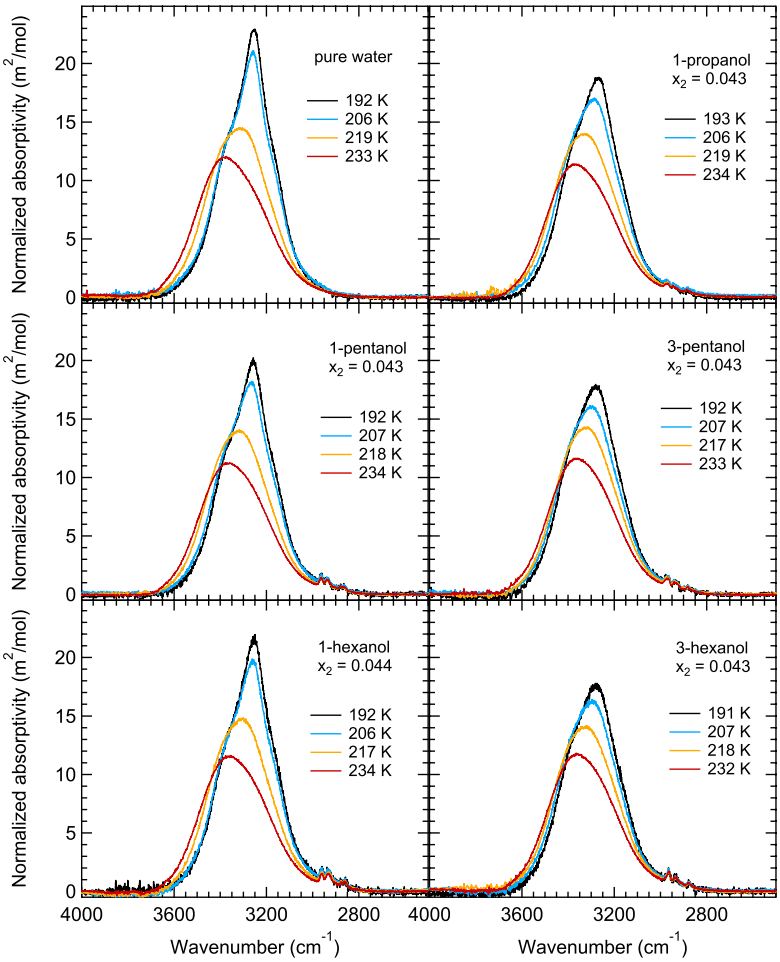

Figure 3 FTIR spectra in the hydrogen bonded OH stretch region of <*r*> ~ 6 nm nanodroplets at selected temperatures for pure water and aqueous-alcohol mixtures at x_2~ 0.043. The spectra at the two higher temperatures correspond to liquid-state aerosols while the spectra at the lowest temperature (~192 K) are taken near the nozzle exit at the lowest temperatures accessible in the experiments. For pure water, 1-pentanol and 1-hexanol this corresponds to the fully frozen aerosol as discussed in more detail in Sec. III.C.

Approximately 25 temperature resolved spectra were measured for each aqueous-alcohol composition and most of the IR spectra measured as part of this work are available as Figure S3 in the SI. The data sets for pure water, 1-propanol, and 1-pentanol are available in Ref. 18 as Figure 4, Figure S3 and Figure S4. Since IR spectra reflect a molecule's environment and alcohol is expected to enrich the surface, we estimated the time required to equilibrate the droplet structure. Based on droplet size and the diffusivities of components in the liquid state, the time constant is estimated to be ~1 μs, and the droplets should therefore achieve their equilibrium structure by the time condensation is complete (Section SIII.C of Ref. 18). This

result is consistent with the MD simulations of aqueous–1-butanol nanodroplets where the final droplet structures were reached well within the ~100 ns simulation time.[57]

Changes in the OH band shape with composition and temperature, relative to those for pure water, clearly depend both on concentration and the alcohol under consideration. Selected FTIR spectra for pure water and water-alcohol mixtures at x_2~ 0.043 are shown in Figure 3 for temperatures that span the measurement range. This value of x_2 was chosen because it is the highest value for which data are available for all aqueous-alcohol mixtures. The changes in the spectra with temperature – the shift of the peak in the hydrogen bonded OH stretch region to lower wavenumbers summarized in Figure 4 (a), the narrowing of the band, and the rapid increase in intensity shown in Figure 4 (b) – are all indicators that the droplets are cooling and then, potentially, freezing. The red-shift of the OH stretch band as temperature decreases is consistent with increasing H-bond strength between the water molecules, and the final peak position for pure water (3250 cm^{-1}) is highly consistent with both our earlier work[18,44,49] and the ice nanoparticle measurements of Medcraft *et al*.[58] At the lowest temperatures, the presence of alcohol leads to a somewhat broader, less peaked OH band. Despite big differences in solubility, changes in the spectra for the 3-alcohols are closer to those observed for 1-propanol than for the corresponding 1-alcohols. For temperatures less than 220 K, the peak positions remain at higher wavenumber and the rapid increase in peak intensity observed for water and the other 1-alcohols (Figure 4 (b)) in this temperature range is greatly diminished or nonexistent. As illustrated in Figure 5 (a) for 3-pentanol, changes in the lowest temperature spectra (~192 ± 1 K) are more severe at higher alcohol concentrations and, furthermore, there is a rapid shift in peak intensity as x_2 increases from 0.03 to 0.043. For the 3-alcohols, an estimate based on geometric arguments suggest that a full monolayer on 6 nm droplets corresponds to $x_2 \approx 0.024$, whereas for the 1-alcohols this should occur near $x_2 \approx 0.046$. Although the rapid changes in intensity observed in the low temperature spectra, summarized in Figure 5 (b), do not line up perfectly with these estimates, the general trend that the branched alcohols perturb freezing at lower concentrations than the 1-alcohols appears to hold. Although solubility also plays a role, we note that the solubility of 3-hexanol is lower than that of 1-pentanol, yet the former affects freezing at lower x_2 than the latter. Overall, the spectral changes indicate that even at relatively low concentrations the presence of alcohol can delay the time/temperature at which freezing starts, perturb the H-bonding environment, and lead to a final structure that is less ordered than that of pure ice.

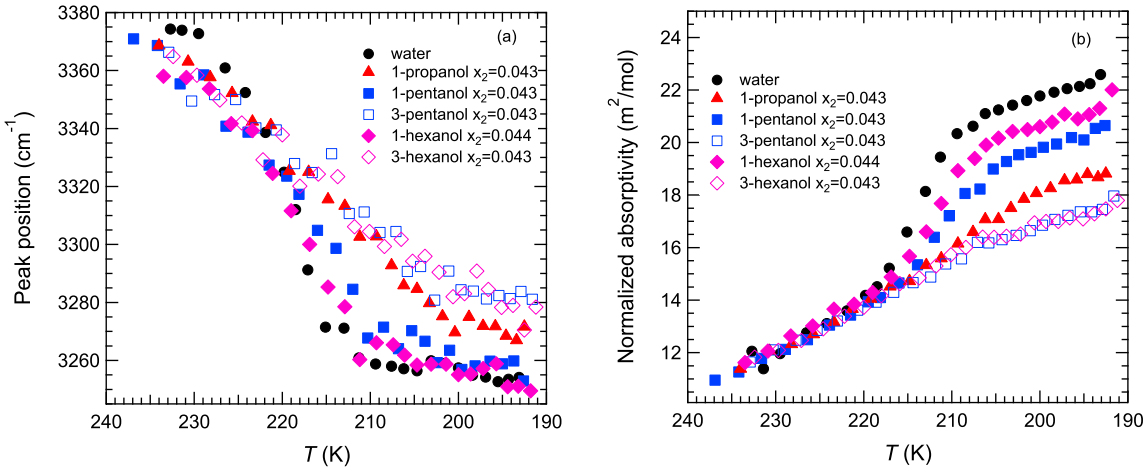

Figure 4 In the hydrogen bonded OH stretch region (a) the peak positions decrease and (b) the peak intensities increase systematically with decreasing temperature. The aqueous-alcohol mixtures all have alcohol concentrations close to x_2=0.043. Both trends are consistent with a stronger H-bonding environment as the particles cool. The higher wavenumber and lower intensity for the aqueous-alcohol mixtures relative to pure water at a fixed temperature suggests slower freezing kinetics and/or the formation of a less ordered structures.

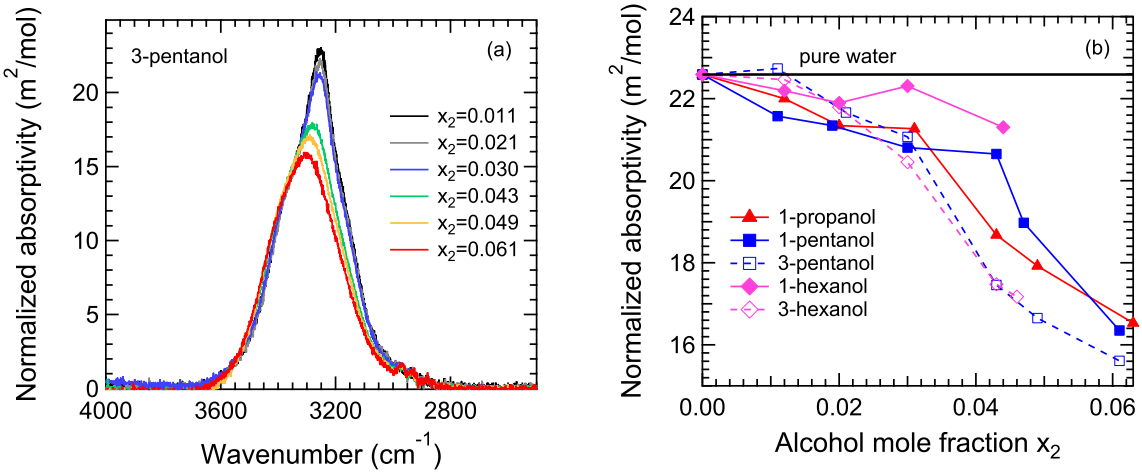

Figure 5 (a) Spectra of aqueous-3-pentanol mixtures at the nozzle exit (~192 K) for the indicated values of x_2. The peak intensity of the OH stretching band decreases and shifts to higher wavenumber as the alcohol concentration increases. **(b)** Changes in the peak intensities of the OH stretching band at 193 ± 0.5 K vary with alcohol concentration. In general, the 3-alcohols exhibit a rapid decrease in peak intensity at lower concentrations than the corresponding 1-alcohols

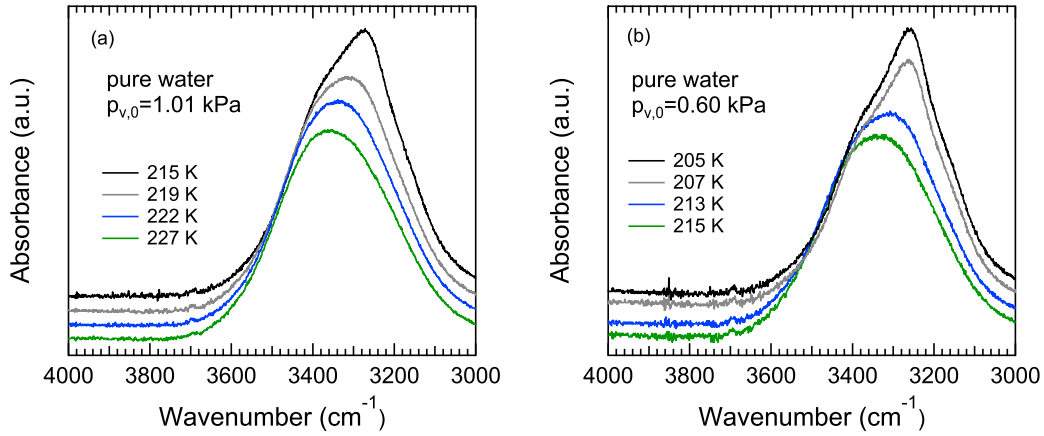

Figure 6 For pure water nanodroplets, the free OH peak at ~ 3690 cm^{-1} of pure water is observed in many of the spectra. The initial water vapor pressures and temperatures are indicated in each figure and the particles in **(a)** ~ 6nm, are larger and warmer than those in **(b)** ~ 5 nm. This peak is very rarely observed in aqueous-alcohol mixtures, consistent with the alcohols displacing H_2O from the surface and hydrogen bonding with the dangling OH of water on the surface. The intensity is arbitrarily increased for clarity. The spectra in (b) are noisier than those in (a) because the particles are smaller in size.

Given the average droplet size ($\langle r \rangle$ ~6 nm), condensable compositions, and the preferential partitioning of the alcohol to the surface, most of the water molecules (> 90%) are in the bulk phase. Thus, most of the signal in the OH stretch region (Figure 3) originates from the droplet interior. Nevertheless, for the pure water droplets, Figure 6 shows that a small peak near ~3690 cm^{-1}, consistent with free OH at the surface of the droplet, is visible in some $\langle r \rangle$ ~6 nm droplet spectra. This peak is also observed for pure water droplets produced at water initial partial pressures of 0.60 kPa, Figure 6(b) and 0.78 kPa, Figure S4, where the particle sizes based on simple scaling arguments[59] should be ~5.0 nm and ~5.5 nm, respectively. For the smaller particles, the peak was observed at temperatures as low as ~205 K, i.e. when droplet freezing is well under way. This peak is only rarely observed at the lowest propanol concentrations, and never observed when the C5/C6 alcohols are present. Since the experimental setup is open to the atmosphere and the vapor phase water lines are suppressed by the FTIR software, this peak could be the result of poor background subtraction brought on by water vapor fluctuations in the air surrounding the nozzle. The sensitivity of this peak to the presence of alcohol, however, argues against this. In particular, the free OH peak signals the existence of unbonded hydrogen that arises on the droplet surface, and it is routinely observed in IR spectra of ice nanoparticles.[58,60] The spectra of water clusters, calculated using a quantum mechanical model, show the free OH peak for clusters containing as few as 20 water molecules but the peak blurs out for bulk systems when the 4-coordinated crystal core grows.[61] Nanodroplets possess a large surface area relative to their volume that, coupled with the high aerosol number density and low temperatures, favors the emergence of this peak. The disappearance of the free OH peak in the presence of the alcohols suggests a reduction in the unbonded OH, consistent with the alcohols displacing water from the droplet surface and the alcohol OH group hydrogen bonding to the uncoordinated H of water. The disappearance of this peak therefore provides additional

evidence for the surface partitioning propensity of the amphiphilic molecules.

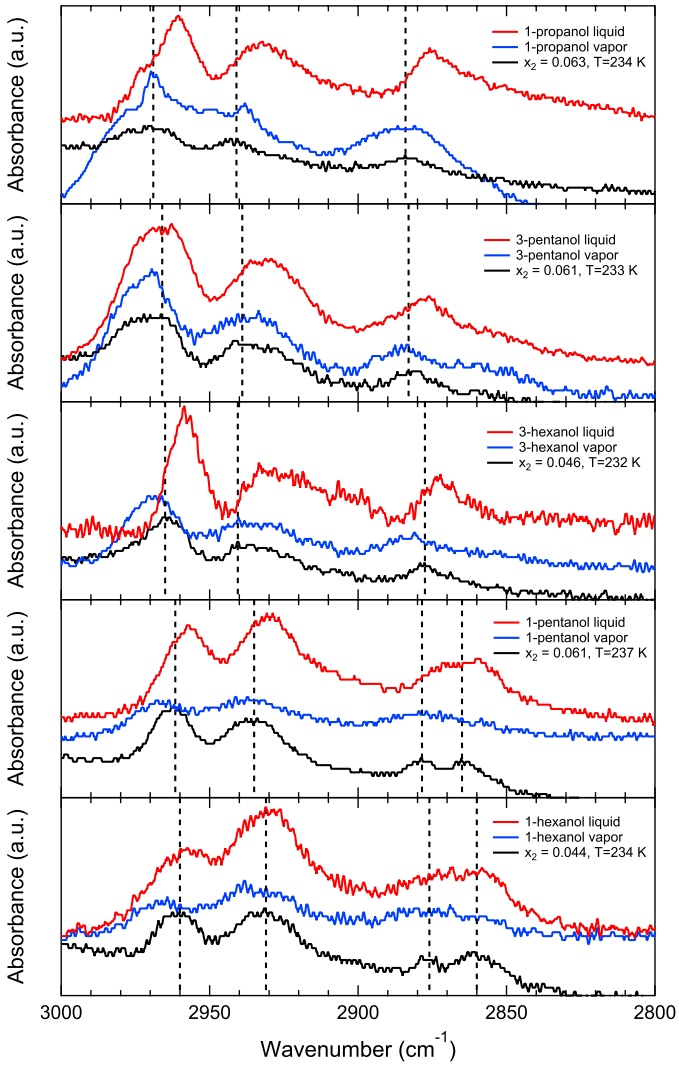

Figure 7 IR spectra for pure alcohol liquid droplets (red), vapor (blue), and the aqueous-alcohol droplets (black) at the noted compositions. For the aqueous-alcohol droplets the locations of the CH stretch peaks are not sensitive to the composition or temperature over the accessible experimental range (see Figure S6 and Figure S7), and thus, representative but clean spectra are shown. The spectra are presented in order of increasing alkyl segment length(s) attached to the -OH carbon and illustrate a gradual shift from peaks that are more aligned with the vapor spectra to those that are more closely aligned with the liquid spectra.

In contrast to the water signal, partitioning calculations and XPS experiments[25] suggest that the CH stretch signal, in the range of 3000-2800 cm^{-1}, originates largely from alcohol molecules residing on the surface of the aqueous alcohol droplets. Even for the miscible 1-propanol, we estimate that at $x_2 = 0.06$, more than 70% of the alcohol segregates to the droplet surface.[18] If the number of molecules on the surface is limited by the available surface area and the alcohol's molecular footprint, then we would expect the C5/C6 1-alcohols (surface area per molecule[25] ~0.4 nm^2) to exhibit higher surface partitioning and stronger intermolecular interactions than

their 3-alcohol counterparts (surface areas per molecule[25] ~ 0.6 nm^2).

Figure 7 illustrates the spectra in the CH stretch region measured for the aqueous-alcohol droplets at the highest alcohol concentrations as well as spectra corresponding to the pure vapor and to liquid nanodroplets. The pure alcohol spectra were measured by producing particles in the nozzle in the absence of water. Spectra measured before nucleation occurs correspond to the pure vapor state of the alcohol, and those taken further downstream are dominated by the condensed liquid. In general, the locations of the CH stretch bands are not expected to be very temperature sensitive[62] but they do depend on the phase, i.e. liquid vs vapor. As expected (Figure S5), the vapor phase alcohol spectra do not contain features in the intermolecular OH stretch region (3600-3000 cm^{-1}) because at the low vapor phase concentrations used here, the alcohol molecules do not form enough small gas phase clusters (dimers, tetramers, etc.) via H-bonding to be detected. As the alcohols nucleate and grow to form small droplets the OH stretch band emerges (Figure S5) and the CH peaks for the liquid redshift from the vapor phase peaks by about 5-8 cm^{-1}, consistent with stronger interactions between the alkyl groups.

As illustrated in Figure S6 and Figure S7, the CH peak locations in the aqueous alcohol droplet spectra are not sensitive to composition or temperature over the accessible measurement range, i.e. when signals are strong enough for peaks to be easily identified. The CH peaks do, however, move from aligning closely with the vapor alcohol peaks (water-1-propanol) to aligning closely with the liquid alcohol peaks (water-1-hexanol) as the length of the alkane segment(s) relative to the position of the -OH carbon, increases. We interpret the alignment between the CH peaks measured for the aqueous-alcohol droplet and the vapor alcohol peaks to indicate that the alcohol molecules are isolated from each other – either because they are more spread out on the surface or solvated in the interior of the droplets. For 1-propanol, our results are consistent with bulk aqueous 1-propanol mixture measurements of Max *et al.*[63] and Tong *et al*.[64] In particular, the peaks we observe line up well with the values Max *et al*. assigned to the 1-propanol-H_2O hydrate, and with those measured by Tong *et al.* in dilute 1-propanol solutions. Furthermore, Tong *et al.* reported that for dilute alcohol mixtures the peak locations did not depend strongly on concentration. In general, the blue shifts in the CH stretch frequencies relative to the pure liquid peaks are attributed to weakened interactions between alkyl groups. In contrast, for the aqueous-alcohol droplets with the longest hydrocarbon chain (1-hexanol), the CH peak positions are more consistent with the corresponding pure liquid peaks. We interpret this as indicating that very few alcohol molecules are solvated and more are aligned on the droplet surface, mimicking the interactions of the liquid alcohol. Unfortunately, we are not aware of any IR measurements on dilute aqueous solutions of the longer chain alcohols with which we could directly compare our results. Similar changes in peak positions with increasing concentration have been reported for bulk *tert*-butanol solutions, where the red-shift of the CH peaks when alcohol concentrations increase above $x_2 = 0.025$ reflects the increasing self-aggregation of the alcohol molecules.[65]

C. SMCR Analysis and the kinetics of freezing

In our previous paper,[18] we applied two rounds of SMCR analysis to each set of temperature dependent spectra corresponding to a fixed alcohol composition to extract both the LTL and the IC spectra. For pure water and a given alcohol, the LTL spectra were independent of the alcohol concentration over the entire range investigated, and when the alcohol concentrations were below a critical value, the IC spectra were essentially identical to those for pure water. We interpreted the latter to mean that the ice formed in the aqueous-alcohol droplets was the same as that formed in pure water droplets. Finally, none of the extracted IC spectra were significantly changed by small shifts in the temperature of the HTL reference spectrum or the temperature range used to determine the LTL spectra (Figure S8 of Ref. 18).

In this paper we apply the same approach to examine the effect alcohol isomerization has on freezing, and to further test our hypothesis that the 3-alcohols with their larger molecular footprint could impact ice formation at lower concentrations than the 1-alcohols in a way that contradicts our expectations based solely on solubility. The first round of SMCR yields the composite LTL liquid spectrum and, as illustrated in Figure 8 for the fixed alcohol concentration $x_2 \approx 0.043$, the main LTL peak (ignoring CH bands) is insensitive to the type of alcohol present even though the HTL reference spectra clearly differ. As in our previous work, the LTL spectra (Figure S8) for a given alcohol are essentially independent of the alcohol concentration. Both observations suggest that changes to the temperature dependence of the liquid droplet spectra are largely driven by changes in the hydrogen bonding between water molecules.

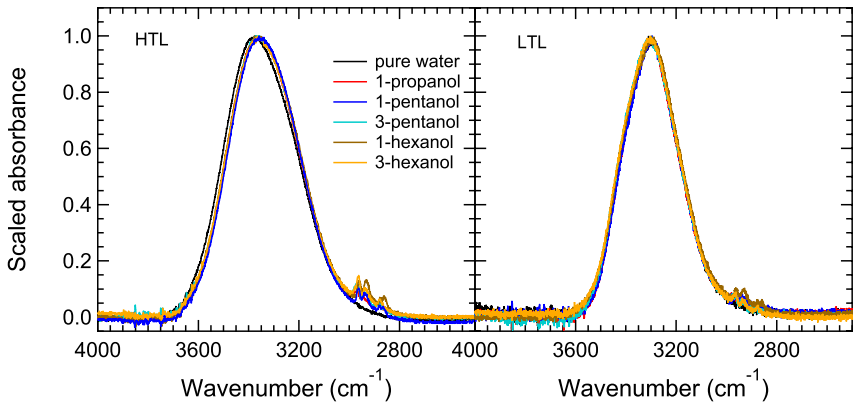

Figure 8 HTL reference spectra for water and aqueous-alcohol mixtures at $x_2 \approx 0.043$ and LTL spectra derived from SMCR analysis. Intensities are scaled to 1 for easier comparison. LTL spectra all exhibit the same shape even though the HTL references differ as the alcohol changes.

Changes in the IC spectra with composition are summarized in the left-hand panel of Figure 9 for all the alcohols investigated. As in our previous work, for each alcohol there is a critical composition (denoted by a *) below which the IC is the same as that for pure water. For a given molecular structure, i.e. linear or branched, the critical composition increases as the solubility decreases. But for different isomers, solubility alone may not predict the observed behavior. In particular, the critical concentration for 3-hexanol is lower than that of 1-pentanol even though

3-hexanol is less soluble than 1-pentanol. This behavior is in line with our hypothesis that molecules with a larger molecular footprint can be forced into the droplet interior once the surface is saturated. Perhaps more surprising – and more difficulty to rationalize – is the observation that 1-propanol's critical concentration is higher than that of 3-pentanol even though the former is fully miscible at room temperature and the latter is not. One issue that is difficult to address, but that may play a role, is the rapid increase in solubility with decreasing temperature for 3-pentanol illustrated in Figure S1. Since freezing is generally initiated near 220 K, it may be that 3-pentanol is fully miscible – or close to it – under these conditions. If increases in solubility change the partitioning behavior and lead to comparable bulk compositions for these two species, then the larger molecular volume of 3-pentanol should perturb freezing more readily. Unfortunately, in the absence of relevant physical property data, especially composition and temperature dependent surface tension data, this observation cannot yet be fully explained using partitioning models.[18] Molecular dynamics simulations that explore the delicate balance that establishes the distribution of molecules within the confined environment of a nanodroplet, especially as temperature, composition, and molecular structure are varied, are one way forward. Such calculations are, however, outside the scope of the current work.

For concentrations below the critical value, the change in the fraction of unfrozen droplets ($\ln(1-F_F)$) is plotted as a function of time in the right-hand panel. When the IC deviates from that of pure water, it is not clear whether ice is forming fast enough to ensure the assumptions inherent in Eq. (2) hold or if pure ice is forming at all. Thus, for these cases it is not reasonable to estimate F_F from F_{IC}. For the $\langle r \rangle \cong 6$ nm droplets used here, the ice nucleation rates for all conditions are bounded by that for pure water nanodroplets where $J_{ice} = 7.5\times10^{22}$ $cm^{-3}s^{-1}$ and that for aqueous propanol nanodroplets at x_2=0.031 where $J_{ice} = 3.4\times10^{22}$ $cm^{-3}s^{-1}$. As the alcohol mole fraction increases, the onset of freezing also occurs further downstream at lower temperatures relative to pure water, in accordance with the expected colligative behavior. For the C5/C6 isomers, Walz *et al.*[25] measured surface:bulk concentration ratios on the order of 100:1. Thus, even if most of the alcohol molecules reside on the surface and do not disturb the nanodroplet freezing, a small fraction of the molecules can dissolve in the bulk and depress the freezing temperature. The fact that the kinetics of freezing are not greatly affected simply reflects the fact that the time available for ice nucleation within the nozzle is ~50 μs. Thus, for freezing to be observed in such small droplets means that the ice nucleation rates must be on the order of 10^{22} $cm^{-3}s^{-1}$.

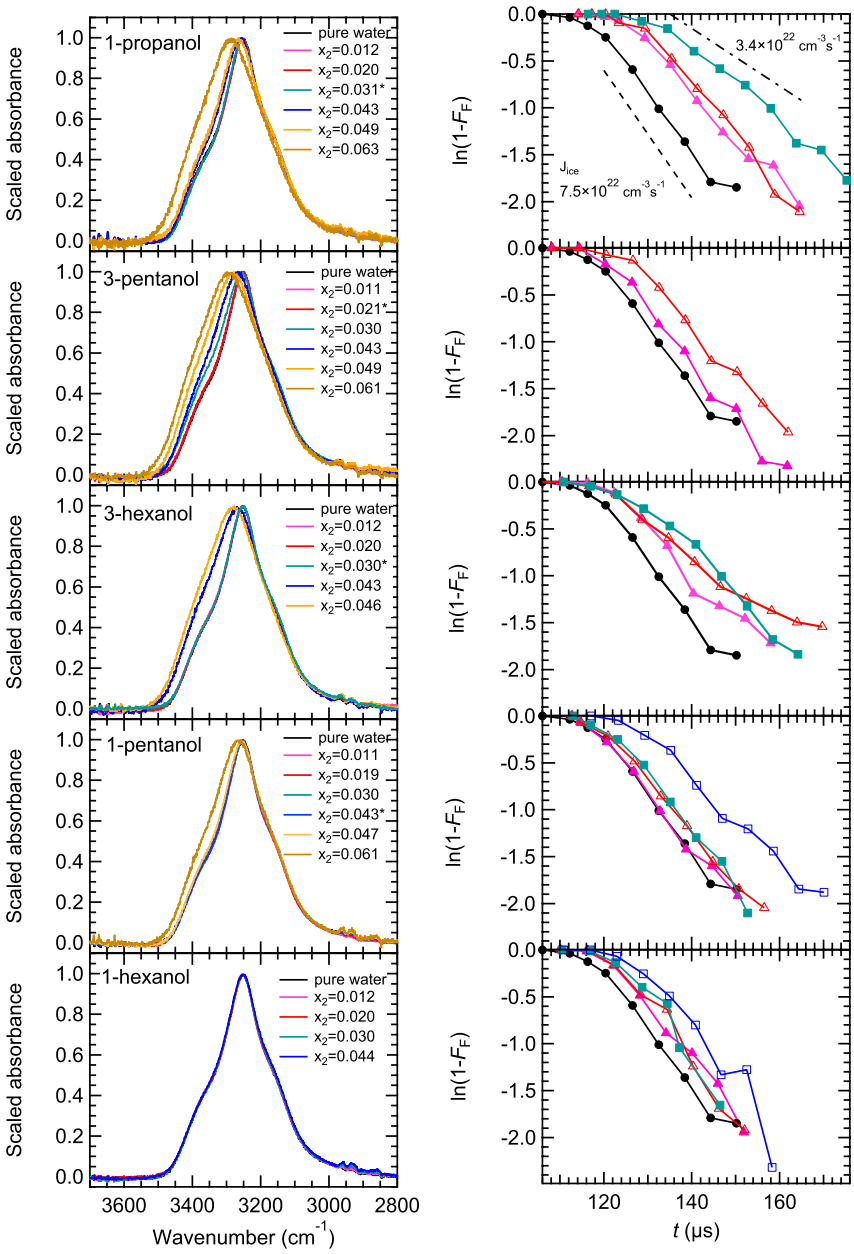

Figure 9 (left panel) The IC spectra derived from two rounds of SMCR analysis for aqueous-alcohol mixtures at all investigated concentrations are compared to the IC spectrum for pure water. The IC spectra broaden and shift to higher wavenumber once x_2 exceeds a threshold value (denoted by *), suggesting that a structure less ordered than pure ice has formed. The data are presented in order of increasing alkyl segment length(s) attached to the -OH carbon. **(right panel)** The freezing kinetics are evaluated for alcohol concentrations where the IC spectra closely match that of pure water. For these aqueous alcohol droplets, the slope of ln(1-F_F) versus the aerosol travel time t relative to the effective throat is proportional to the nucleation rate. The 1-propanol and 1-pentanol data are reproduced from Ref. 18 with permission from the PCCP Owner Societies.

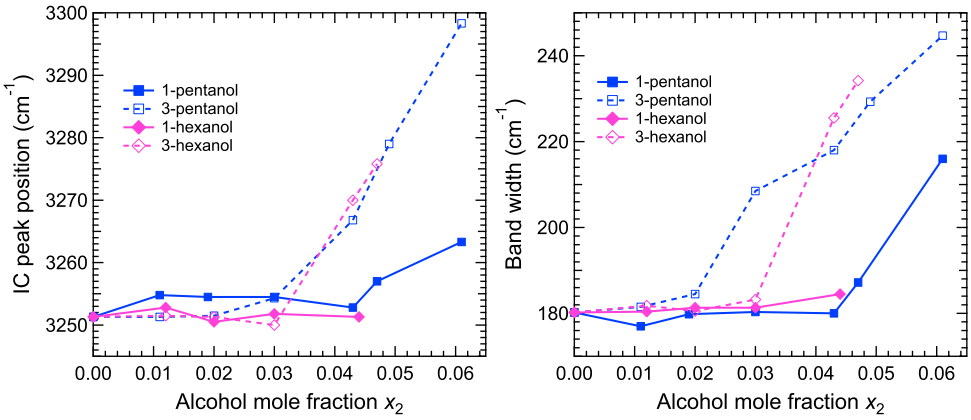

Figure 10. Both the IC component peak position and bandwidth indicate that 3-alcohols start to perturb the highly-ordered ice structure at lower concentrations than their terminal counterparts.

Figure 5(b) already indicated that the 3-alcohols perturbed freezing at lower concentrations than the corresponding 1-alcohols. This effect is, however, demonstrated more clearly by changes in the properties of the IC spectra illustrated in Figure 10. Here the thresholds for the blue-shift and broadening of the IC spectra are clearly separated between the corresponding branched and terminal alcohols. If surface partitioning of the alcohol molecules were unimportant, one might expect changes in the IC spectra to more closely follow the miscibility trends for these alcohols, i.e. the most soluble 3-pentanol disturbing the H-bonding network more readily than 1-pentanol, 3-hexanol and 1-hexanol. The SMCR results, however, show that both branched alcohols appear to affect the IC spectra in a similar manner and at lower concentrations than the linear alcohols, a trend that is consistent with their respective molecular areas at monolayer coverage (See Table 1). In particular, the molecular areas of the 3-alcohols (~60 Å^2) are systematically larger than their corresponding 1-alcohols (~40 Å^2). Thus, fewer 3-alcohol molecules can be accommodated on the surface before being forced into the bulk where they can interfere with ice formation. Comparing the two branched alcohols, the addition of 3-pentanol broadens the IC spectrum at a concentration slightly lower than 3-hexanol. This is consistent with a slight difference in molecular areas, but more likely reflects 3-pentanol's higher solubility in water especially as temperature decreases. Similar comparison of the 1-alcohols is difficult since experiments with 1-hexanol were limited to mole fractions below 0.044 where the IC is still essentially identical to that of pure water. Even though the FTIR measurements do not provide direct information regarding the droplet surface, the SMCR results do reflect the partitioning propensities of the series of alcohols. Molecular dynamics simulations could provide additional insight into the competing effects that temperature dependent solubility and surface accommodation have on freezing especially in the context of the highly curved surfaces and confined environment that are characteristic of nanodroplets.

IV. Summary and Conclusions

We examined how low concentrations ($x_2 \leq 0.06$) of the 1- and 3- isomers of pentanol and hexanol affect the freezing of aqueous nanodroplets. The nanodroplets were generated via vapor-liquid nucleation in a supersonic nozzle and the phase transitions were characterized using PTM and FTIR measurements. At equal alcohol mole fraction, the vapor-to-liquid phase transition is enhanced as the alcohol equilibrium vapor pressure and surface tension decrease. Droplet nucleation and growth are essentially complete in about 20 μs, after which the droplets again cool and, potentially, freeze. At low enough alcohol concentrations, IR measurements in the hydrogen bonded OH stretch region exhibit changes consistent with a clear transition from the liquid to the solid state. As the alcohol concentration increases, the band intensity decreases sharply relative to that observed for pure water and the band widens; it is no longer clear whether ice forms.

In our earlier work with 1-pentanol the abrupt change in spectral shape with increasing alcohol concentration occurred close to an alcohol mole fraction where simple geometric arguments suggest the surface was saturated with the alcohol. Here we find that these changes occur at lower alcohol mole fraction for the 3-alcohols (x_2~ 0.03) than the corresponding 1-alcohols (x_2~ 0.044). These changes are consistent with the larger solubility and molecular footprints of the branched isomers relative to their straight chain counterparts.

The measured spectra were also decomposed into HTL, LTL and IC spectral components using two rounds of SMCR analysis. Even when the HTL spectra vary, under our experimental conditions the LTL spectra are remarkably consistent and independent of the concentration or the alcohol under consideration. Below a threshold alcohol concentration, the IC spectra closely resemble that of pure water ice suggesting that the ice formed is the same as that produced when pure water freezes. The threshold concentration above which the IC starts to deviate from that of the pure water is lower for the branched alcohols than the terminal alcohols, and for a particular molecular structure, the critical composition increases as the solubility decreases. Comparing between isomers, we found that the critical concentration for 3-hexanol is lower than that of 1-pentanol even though 3-hexanol is less soluble than 1-pentanol. This behavior is consistent with their respective molecular areas. More difficult to explain is the observation that 3-pentanol has a lower critical composition than the fully miscible 1-propanol. Without physical property data, i.e. temperature dependent surface tension measurements for the branched isomers, it is difficult to estimate how partitioning of these molecules changes with temperature. Insight from MD simulations exploring how the distribution of alcohol within the liquid droplets changes with temperature would be an extremely valuable first step toward simulations that consider the freezing process itself. Freezing kinetics are derived when the IC spectra match that of pure water. The results show that temperature at which freezing is initiated decreases when alcohol is present, but that the ice nucleation rates decrease by less than a factor of 2.

For pure water aerosols – both liquid and partially frozen – we observed a small peak at ~ 3690 cm^{-1} that is assigned to the free OH peak at the air-water interface.[61,66,67] The disappearance of

this peak for aqueous-alcohol mixtures is attributed to the displacement of water from the surface by the alcohol molecules as well as H-bonding between the alcohol OH and the unbonded H of water. The systematic red shifts observed in the CH stretch peaks as the alkyl segment length(s) increase, relative to the OH bonded carbon, also suggest that fewer alcohol molecules are solvated in the bulk of the droplet and more are aggregating on the surface as these hydrophobic regions increase.

Associated Content

Summary of the physical properties; Experiment apparatus; more extensive FTIR results

Acknowledgements

This work was completed with the financial support of the National Science Foundation under grant number CHE-1900064. This research used resources of the Advanced Photon Source, a U.S. Department of Energy (DOE) Office of Science User Facility operated for the DOE Office of Science by Argonne National Laboratory under Contract No. DE-AC02-06CH11357. The authors thank D. Ben-Amotz for providing the SMCR analysis program, teaching us how to use it and for useful discussions.

Table 2: Experimental conditions and results of PTM for (a) water-3-pentanol (b) water 1-hexanol. (c) water 1-hexanol. $\dot{m}$ is the mass flow rate, x is the mole fraction of the alcohol in the condensable material (excluding carrier gas), y_0 is the initial mole fraction in the vapor phase (including carrier gas), p_0 is the initial partial pressure, $T_{\min}$ and $p_{\min}$ are the minimum temperature and pressure within the nucleation pulse, S_i is the supersaturation of the vapor with respect to the pure liquid at $T_{\min}$. for species i. All expansions started from p_0 = 60.0 kPa and T_0 = 35 °C.

(a) Water and 3-pentanol

$\dot{m}_{H_2O}$ (g/min)	$\dot{m}_{3-PenOH}$ (g/min)	$x_{3-PenOH} \times 100$	$y_{0,H2O} \times 100$	$y_{0,3-PenOH} \times 100$	p_{0,H_2O} (kPa)	$p_{0,3-PenOH}$ (kPa)	$T_{\min}$ (K)	$p_{\min,H_2O}$ (kPa)	$p_{\min,3-PenOH}$ (kPa)	S_{H_2O}	$S_{3-PenOH}$
5.50	0.30	1.1	1.59	0.018	0.95	0.011	223.2	0.28	0.003	45	11
5.51	0.58	2.1	1.59	0.034	0.95	0.020	225.6	0.30	0.006	36	15
5.50	0.83	3.0	1.59	0.049	0.95	0.029	228.2	0.30	0.009	27	14
5.51	1.20	4.3	1.59	0.071	0.95	0.042	231.0	0.32	0.014	21	14
5.52	1.38	4.9	1.59	0.081	0.96	0.049	232.4	0.33	0.017	19	14
5.51	1.76	6.1	1.59	0.104	0.95	0.062	234.5	0.34	0.022	16	13

(b) Water and 1-hexanol

$\dot{m}_{H_2O}$ (g/min)	$\dot{m}_{1-hexanol}$ (g/min)	$x_{1-hexanol} \times 100$	$y_{0,H2O} \times 100$	$y_{0,1-hexanol} \times 100$	p_{0,H_2O} (kPa)	$p_{0,1-hexanol}$ (kPa)	$T_{\min}$ (K)	$p_{\min,H_2O}$ (kPa)	$p_{\min,1-hexanol}$ (kPa)	S_{H_2O}	$S_{1-hexanol}$
5.51	0.38	1.2	1.60	0.020	0.96	0.012	227.8	0.32	0.004	30	98

5.50	0.64	2.0	1.60	0.032	0.96	0.019	231.9	0.33	0.007	20	94
5.50	0.98	3.0	1.60	0.050	0.96	0.030	236.6	0.35	0.011	13	80
5.51	1.45	4.4	1.60	0.074	0.96	0.045	241.0	0.37	0.017	9.0	68

(c) Water and 3-hexanol

$\dot{m}_{H_2O}$ (g/min)	$\dot{m}_{3-\text{hexanol}}$ (g/min)	$x_{3-\text{hexanol}} \times 100$	$y_{0,H2O} \times 100$	$y_{0,3-\text{hexanol}} \times 100$	p_{0,H_2O} (kPa)	$p_{0,3-\text{hexanol}}$ (kPa)	$T_{\min}$ (K)	$p_{\min,H_2O}$ (kPa)	$p_{\min,3-\text{hexanol}}$ (kPa)	S_{H_2O}	$S_{3-\text{hexanol}}$
5.51	0.38	1.2	1.60	0.020	0.96	0.012	227.0	0.32	0.004	33	28
5.50	0.62	2.0	1.60	0.032	0.96	0.019	231.4	0.32	0.006	20	24
5.51	0.97	3.0	1.60	0.050	0.96	0.030	235.3	0.34	0.011	14	22
5.53	1.40	4.3	1.60	0.072	0.96	0.043	239.1	0.36	0.016	10	20
5.51	1.52	4.6	1.60	0.078	0.96	0.047	240.0	0.38	0.018	10	20

References

(1) Saxena, P.; Hildemann, L. M. Water-Soluble Organics in Atmospheric Particles: A Critical Review of the Literature and Application of Thermodynamics to Identify Candidate Compounds. *J. Atmospheric Chem.* **1996**, *24*, 57–109.

(2) Kanakidou, M.; Seinfeld, J. H.; Pandis, S. N.; Barnes, I.; Dentener, F. J.; Facchini, M. C.; Dingenen, R. V.; Ervens, B.; Nenes, A.; Nielsen, C. J. Organic Aerosol and Global Climate Modelling: A Review. *Atmospheric Chem. Phys.* **2005**, *5*, 1053–1123.

(3) Cruz, C. N.; Pandis, S. N. A Study of the Ability of Pure Secondary Organic Aerosol to Act as Cloud Condensation Nuclei. *Atmos. Environ.* **1997**, *31*, 2205–2214.

(4) Cooke, W. F.; Liousse, C.; Cachier, H.; Feichter, J. Construction of a 1$\times$ 1 Fossil Fuel Emission Data Set for Carbonaceous Aerosol and Implementation and Radiative Impact in the ECHAM4 Model. *J. Geophys. Res. Atmospheres* **1999**, *104*, 22137–22162.

(5) Ng, N. L.; Canagaratna, M. R.; Zhang, Q.; Jimenez, J. L.; Tian, J.; Ulbrich, I. M.; Kroll, J. H.; Docherty, K. S.; Chhabra, P. S.; Bahreini, R. Organic Aerosol Components Observed in Northern Hemispheric Datasets from Aerosol Mass Spectrometry. *Atmospheric Chem. Phys.* **2010**, *10*, 4625–4641.

(6) Ervens, B.; Turpin, B. J.; Weber, R. J. Secondary Organic Aerosol Formation in Cloud Droplets and Aqueous Particles (AqSOA): A Review of Laboratory, Field and Model Studies. *Atmospheric Chem. Phys.* **2011**, *11*, 11069–11102.

(7) Suda, S. R.; Petters, M. D.; Yeh, G. K.; Strollo, C.; Matsunaga, A.; Faulhaber, A.; Ziemann,

P. J.; Prenni, A. J.; Carrico, C. M.; Sullivan, R. C. Influence of Functional Groups on Organic Aerosol Cloud Condensation Nucleus Activity. *Environ. Sci. Technol.* **2014**, *48*, 10182–10190.

(8) Levinger, N. E. Water in Confinement. *Science* **2002**, *298*, 1722–1723.

(9) Werner, J.; Dalirian, M.; Walz, M.-M.; Ekholm, V.; Wideqvist, U.; Lowe, S. J.; Öhrwall, G.; Persson, I.; Riipinen, I.; Björneholm, O. Surface Partitioning in Organic–Inorganic Mixtures Contributes to the Size-Dependence of the Phase-State of Atmospheric Nanoparticles. *Environ. Sci. Technol.* **2016**, *50*, 7434–7442.

(10) Hensel, J. K.; Carpenter, A. P.; Ciszewski, R. K.; Schabes, B. K.; Kittredge, C. T.; Moore, F. G.; Richmond, G. L. Molecular Characterization of Water and Surfactant AOT at Nanoemulsion Surfaces. *Proc. Natl. Acad. Sci.* **2017**, *114*, 13351–13356.

(11) Pagenkopp, M. J.; Mason, T. G. Surfactant Partitioning in Nanoemulsions. *Langmuir* **2018**, *34*, 10309–10320.

(12) Malila, J.; Prisle, N. L. A Monolayer Partitioning Scheme for Droplets of Surfactant Solutions. *J. Adv. Model. Earth Syst.* **2018**, *10*, 3233–3251.

(13) Singh, H.; Chen, Y.; Staudt, A.; Jacob, D.; Blake, D.; Heikes, B.; Snow, J. Evidence from the Pacific Troposphere for Large Global Sources of Oxygenated Organic Compounds. *Nature* **2001**, *410*, 1078–1081.

(14) Davies, J. F.; Miles, R. E. H.; Haddrell, A. E.; Reid, J. P. Influence of Organic Films on the Evaporation and Condensation of Water in Aerosol. Proceedings of the National Academy of Sciences of the United States of America, 110 (22), 8807-8812.

(15) Li, Z.; Williams, A. L.; Rood, M. J. Influence of Soluble Surfactant Properties on the Activation of Aerosol Particles Containing Inorganic Solute. *J. Atmospheric Sci.* **1998**, *55*, 1859–1866.

(16) Sorjamaa, R.; Laaksonen, A. The Influence of Surfactant Properties on Critical Supersaturations of Cloud Condensation Nuclei. *J. Aerosol Sci.* **2006**, *37*, 1730–1736.

(17) Prisle, N. L.; Raatikainen, T.; Laaksonen, A.; Bilde, M. Surfactants in Cloud Droplet Activation: Mixed Organic-Inorganic Particles. *Atmospheric Chem. Phys.* **2010**, *10*, 5663–5683.

(18) Sun, T.; Ben-Amotz, D.; Wyslouzil, B. E. The Freezing Behavior of Aqueous N-Alcohol Nanodroplets. *Phys. Chem. Chem. Phys.* **2021**, *23*, 9991–10005.

(19) Du, Q.; Superfine, R.; Freysz, E.; Shen, Y. R. Vibrational Spectroscopy of Water at the Vapor/Water Interface. *Phys. Rev. Lett.* **1993**, *70*, 2313.

(20) Zhuang, X.; Miranda, P. B.; Kim, D.; Shen, Y. R. Mapping Molecular Orientation and Conformation at Interfaces by Surface Nonlinear Optics. *Phys. Rev. B* **1999**, *59*, 12632.

(21) Richmond, G. L. Molecular Bonding and Interactions at Aqueous Surfaces as Probed by Vibrational Sum Frequency Spectroscopy. *Chem. Rev.* **2002**, *102*, 2693–2724.

(22) Hsieh, C.-S.; Campen, R. K.; Okuno, M.; Backus, E. H.; Nagata, Y.; Bonn, M. Mechanism of Vibrational Energy Dissipation of Free OH Groups at the Air–Water Interface. *Proc. Natl. Acad. Sci.* **2013**, *110*, 18780–18785.

(23) Werner, J.; Julin, J.; Dalirian, M.; Prisle, N. L.; Öhrwall, G.; Persson, I.; Björneholm, O.; Riipinen, I. Succinic Acid in Aqueous Solution: Connecting Microscopic Surface Composition and Macroscopic Surface Tension. *Phys. Chem. Chem. Phys.* **2014**, *16*, 21486–21495.

(24) Walz, M.-M.; Caleman, C.; Werner, J.; Ekholm, V.; Lundberg, D.; Prisle, N. L.; Öhrwall, G.; Björneholm, O. Surface Behavior of Amphiphiles in Aqueous Solution: A Comparison between Different Pentanol Isomers. *Phys. Chem. Chem. Phys.* **2015**, *17*, 14036–14044.
(25) Walz, M.-M.; Werner, J.; Ekholm, V.; Prisle, N. L.; Öhrwall, G.; Björneholm, O. Alcohols at the Aqueous Surface: Chain Length and Isomer Effects. *Phys. Chem. Chem. Phys.* **2016**, *18*, 6648–6656.
(26) Lee, M.-T.; Orlando, F.; Artiglia, L.; Chen, S.; Ammann, M. Chemical Composition and Properties of the Liquid–Vapor Interface of Aqueous C1 to C4 Monofunctional Acid and Alcohol Solutions. *J. Phys. Chem. A* **2016**, *120*, 9749–9758.
(27) Dixit, S.; Crain, J.; Poon, W. C. K.; Finney, J. L.; Soper, A. K. Molecular Segregation Observed in a Concentrated Alcohol–Water Solution. *Nature* **2002**, *416*, 829–832.
(28) Perera, P. N.; Fega, K. R.; Lawrence, C.; Sundstrom, E. J.; Tomlinson-Phillips, J.; Ben-Amotz, D. Observation of Water Dangling OH Bonds around Dissolved Nonpolar Groups. *Proc. Natl. Acad. Sci.* **2009**, *106*, 12230–12234.
(29) Juurinen, I.; Pylkkanen, T.; Sahle, C. J.; Simonelli, L.; Hämäläinen, K.; Huotari, S.; Hakala, M. Effect of the Hydrophobic Alcohol Chain Length on the Hydrogen-Bond Network of Water. *J. Phys. Chem. B* **2014**, *118*, 8750–8755.
(30) Lam, R. K.; Smith, J. W.; Saykally, R. J. *Communication: Hydrogen Bonding Interactions in Water-Alcohol Mixtures from X-Ray Absorption Spectroscopy*; AIP Publishing LLC, 2016.
(31) Lenton, S.; Rhys, N. H.; Towey, J. J.; Soper, A. K.; Dougan, L. Temperature-Dependent Segregation in Alcohol–Water Binary Mixtures Is Driven by Water Clustering. *J. Phys. Chem. B* **2018**, *122*, 7884–7894.
(32) Gliński, J.; Chavepeyer, G.; Platten, J.-K.; Smet, P. Surface Properties of Diluted Aqueous Solutions of Normal Short-Chained Alcohols. *J. Chem. Phys.* **1998**, *109*, 5050–5053.
(33) Ballal, D.; Chapman, W. G. Hydrophobic and Hydrophilic Interactions in Aqueous Mixtures of Alcohols at a Hydrophobic Surface. *J. Chem. Phys.* **2013**, *139*, 114706.
(34) Henry, D. J.; Dewan, V. I.; Prime, E. L.; Qiao, G. G.; Solomon, D. H.; Yarovsky, I. Monolayer Structure and Evaporation Resistance: A Molecular Dynamics Study of Octadecanol on Water. *J. Phys. Chem. B* **2010**, *114*, 3869–3878.
(35) Mondal, J. A.; Namboodiri, V.; Mathi, P.; Singh, A. K. Alkyl Chain Length Dependent Structural and Orientational Transformations of Water at Alcohol–Water Interfaces and Its Relevance to Atmospheric Aerosols. *J. Phys. Chem. Lett.* **2017**, *8*, 1637–1644.
(36) Donaldson, D. J.; Anderson, D. Adsorption of Atmospheric Gases at the Air- Water Interface. 2. C1- C4 Alcohols, Acids, and Acetone. *J. Phys. Chem. A* **1999**, *103*, 871–876.
(37) Can, S. Z.; Mago, D. D.; Esenturk, O.; Walker, R. A. Balancing Hydrophobic and Hydrophilic Forces at the Water/Vapor Interface: Surface Structure of Soluble Alcohol Monolayers. *J. Phys. Chem. C* **2007**, *111*, 8739–8748.
(38) Stephenson, R.; Stuart, J.; Tabak, M. Mutual Solubility of Water and Aliphatic Alcohols. *J. Chem. Eng. Data* **1984**, *29*, 287–290.
(39) Mulero, A.; Cachadiña, I.; Sanjuán, E. L. Surface Tension of Alcohols. Data Selection and Recommended Correlations. *J. Phys. Chem. Ref. Data* **2015**, *44*, 033104.
(40) Campagna, M. M.; Hrubỳ, J.; van Dongen, M. E. H.; Smeulders, D. M. J. Homogeneous Water Nucleation: Experimental Study on Pressure and Carrier Gas Effects. *J. Chem. Phys.*

2020, *153*, 164303.
(41) Amaya, A. J. Freezing Supercooled Water Nanodroplets near ~225 K through Homogeneous and Heterogeneous Ice Nucleation. Ph.D. Dissertation, The Ohio State University, Columbus, 2018.
(42) Wyslouzil, B. E.; Heath, C. H.; Cheung, J. L.; Wilemski, G. Binary Condensation in a Supersonic Nozzle. *J. Chem. Phys.* **2000**, *113*, 7317–7329.
(43) Tanimura, S.; Zvinevich, Y.; Wyslouzil, B. E.; Zahniser, M.; Shorter, J.; Nelson, D.; McManus, B. Temperature and Gas-Phase Composition Measurements in Supersonic Flows Using Tunable Diode Laser Absorption Spectroscopy: The Effect of Condensation on the Boundary-Layer Thickness. *J. Chem. Phys.* **2005**, *122*, 194304.
(44) Manka, A.; Pathak, H.; Tanimura, S.; Wölk, J.; Strey, R.; Wyslouzil, B. E. Freezing Water in No-Man's Land. *Phys. Chem. Chem. Phys.* **2012**, *14*, 4505–4516.
(45) Pattenaude, S. R.; Streacker, L. M.; Ben-Amotz, D. Temperature and Polarization Dependent Raman Spectra of Liquid H2O and D2O. *J. Raman Spectrosc.* **2018**, *49*, 1860–1866.
(46) Morawietz, T.; Marsalek, O.; Pattenaude, S. R.; Streacker, L. M.; Ben-Amotz, D.; Markland, T. E. The Interplay of Structure and Dynamics in the Raman Spectrum of Liquid Water over the Full Frequency and Temperature Range. *J. Phys. Chem. Lett.* **2018**, *9*, 851–857.
(47) Morawietz, T.; Urbina, A. S.; Wise, P. K.; Wu, X.; Lu, W.; Ben-Amotz, D.; Markland, T. E. Hiding in the Crowd: Spectral Signatures of Overcoordinated Hydrogen-Bond Environments. *J. Phys. Chem. Lett.* **2019**, *10*, 6067–6073.
(48) Huang, J.; Bartell, L. S. Kinetics of Homogeneous Nucleation in the Freezing of Large Water Clusters. *J. Phys. Chem.* **1995**, *99*, 3924–3931.
(49) Amaya, A. J.; Wyslouzil, B. E. Ice Nucleation Rates near 225 K. *J. Chem. Phys.* **2018**, *148*, 084501.
(50) Pathak, H.; Mullick, K.; Tanimura, S.; Wyslouzil, B. E. Nonisothermal Droplet Growth in the Free Molecular Regime. *Aerosol Sci. Technol.* **2013**, *47*, 1310–1324.
(51) Park, Y.; Tanimura, S.; Wyslouzil, B. E. Enhanced Growth Rates of Nanodroplets in the Free Molecular Regime: The Role of Long-Range Interactions. *Aerosol Sci. Technol.* **2016**, *50*, 773–780.
(52) Wilemski, G. Revised Classical Binary Nucleation Theory for Aqueous Alcohol and Acetone Vapors. *J. Phys. Chem.* **1987**, *91*, 2492–2498.
(53) Heath, C. H.; Streletzky, K.; Wyslouzil, B. E.; Wölk, J.; Strey, R. H 2 O–D 2 O Condensation in a Supersonic Nozzle. *J. Chem. Phys.* **2002**, *117*, 6176–6185.
(54) Strey, R.; Viisanen, Y.; Wagner, P. E. Measurement of the Molecular Content of Binary Nuclei. III. Use of the Nucleation Rate Surfaces for the Water-n-Alcohol Series. *J. Chem. Phys.* **1995**, *103*, 4333–4345.
(55) Mullick, K. Binary Nucleation of N-Butanol and Deuterium Oxide Conducted in Supersonic Nozzles. Ph.D. Dissertation, The Ohio State University, Columbus, 2012.
(56) Kim, Y. J.; Wyslouzil, B. E.; Wilemski, G.; Wölk, J.; Strey, R. Isothermal Nucleation Rates in Supersonic Nozzles and the Properties of Small Water Clusters. *J. Phys. Chem. A* **2004**, *108*, 4365–4377.
(57) Hrahsheh, F.; Wudil, Y. S.; Wilemski, G. Confined Phase Separation of Aqueous–Organic

Nanodroplets. *Phys. Chem. Chem. Phys.* **2017**, *19*, 26839–26845.
(58) Medcraft, C.; McNaughton, D.; Thompson, C. D.; Appadoo, D. R.; Bauerecker, S.; Robertson, E. G. Water Ice Nanoparticles: Size and Temperature Effects on the Mid-Infrared Spectrum. *Phys. Chem. Chem. Phys.* **2013**, *15*, 3630–3639.
(59) Ghosh, D.; Manka, A.; Strey, R.; Seifert, S.; Winans, R. E.; Wyslouzil, B. E. Using Small Angle X-Ray Scattering to Measure the Homogeneous Nucleation Rates of n-Propanol, n-Butanol, and n-Pentanol in Supersonic Nozzle Expansions. *J. Chem. Phys.* **2008**, *129*, 124302.
(60) Isenor, M.; Signorell, R. Infrared Spectroscopy of Solid Mixed Ammonia–Water and Acetylene–Water Aerosol Particles. *Mol. Phys.* **2015**, *113*, 823–834.
(61) Buch*, V.; Sigurd, B.; Paul Devlin, J.; Buck, U.; Kazimirski, J. K. Solid Water Clusters in the Size Range of Tens–Thousands of H2O: A Combined Computational/Spectroscopic Outlook. *Int. Rev. Phys. Chem.* **2004**, *23*, 375–433.
(62) Modak, V. P.; Pathak, H.; Thayer, M.; Singer, S. J.; Wyslouzil, B. E. Experimental Evidence for Surface Freezing in Supercooled N-Alkane Nanodroplets. *Phys. Chem. Chem. Phys.* **2013**, *15*, 6783–6795.
(63) Max, J.-J.; Daneault, S.; Chapados, C. 1-Propanol Hydrate by IR Spectroscopy. *Can. J. Chem.* **2002**, *80*, 113–123.
(64) Tong, H.-J.; Yu, J.-Y.; Zhang, Y.-H.; Reid, J. P. Observation of Conformational Changes in 1-Propanol- Water Complexes by FTIR Spectroscopy. *J. Phys. Chem. A* **2010**, *114*, 6795–6802.
(65) Freda, M.; Onori, G.; Santucci, A. Infrared Study of the Hydrophobic Hydration and Hydrophobic Interactions in Aqueous Solutions of Tert-Butyl Alcohol and Trimethylamine-N-Oxide. *J. Phys. Chem. B* **2001**, *105*, 12714–12718.
(66) Davis, J. G.; Gierszal, K. P.; Wang, P.; Ben-Amotz, D. Water Structural Transformation at Molecular Hydrophobic Interfaces. *Nature* **2012**, *491*, 582–585.
(67) Deng, G.-H.; Shen, Y.; Chen, H.; Chen, Y.; Jiang, B.; Wu, G.; Yang, X.; Yuan, K.; Zheng, J. Ordered-to-Disordered Transformation of Enhanced Water Structure on Hydrophobic Surfaces in Concentrated Alcohol–Water Solutions. *J. Phys. Chem. Lett.* **2019**, *10*, 7922–7928.

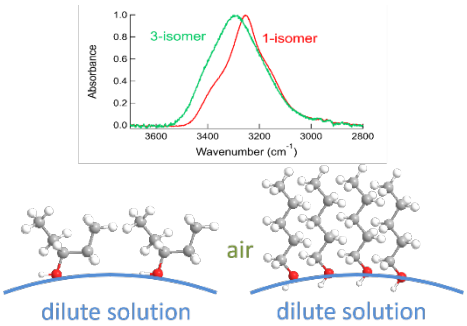
3-isomer
1-isomer
Absorbance
1.0
0.8
0.6
0.4
0.2
0.0
3600
3400
3200
3000
2800
Wavenumber (cm-1)
air
dilute solution
dilute solution